PAPER • OPEN ACCESS

Enhancing ion extraction with an inverse sheath in negative hydrogen ion sources for NBI heating

OPEN ACCESS
IOP Publishing | International Atomic Energy Agency
Nuclear Fusion
Nucl. Fusion **63** (2023) 096022 (15pp)
https://doi.org/10.1088/1741-4326/acec5b

Enhancing ion extraction with an inverse sheath in negative hydrogen ion sources for NBI heating

Guang-Yu Sun[1], Wei Yang[2], Jian Chen[3], Hao-Min Sun[4], Bao-Hong Guo[5], Shu Zhang[1], Ying-Han Wang[4], Xiong Yang[1], An-Bang Sun[1,*] and Guan-Jun Zhang[1,*]

[1] State Key Laboratory of Electrical Insulation and Power Equipment, School of Electrical Engineering, Xi'an Jiaotong University, Xi'an, China
[2] College of Science, Donghua University, Shanghai, 201620, China
[3] Sino-French Institute of Nuclear Engineering and Technology, Sun Yat-sen University, Zhuhai 519082, China
[4] Ecole Polytechnique Fédérale de Lausanne (EPFL), Swiss Plasma Center (SPC), CH-1015 Lausanne, Switzerland
[5] Centrum Wiskunde and Informatica (CWI), Amsterdam, Netherlands

E-mail: anbang.sun@xjtu.edu.cn and gjzhang@xjtu.edu.cn

Received 5 January 2023, revised 19 June 2023
Accepted for publication 1 August 2023
Published 11 August 2023

Abstract

Negative hydrogen ion (H^-) sources employed in neutral beam injection (NBI) systems are subject to extraction efficiency issues due to the considerable volumetric losses of negative hydrogen ions. Here, we propose to improve the H^- extraction by activating an alternative sheath mode, the electronegative inverse sheath, in front of the H^- production surface, which features zero sheath acceleration for H^- with a negative sheath potential opposite to the classic sheath. With the inverse sheath activated, the produced H^- exhibits smaller gyration, a shorter transport path, less destructive collisions, and therefore higher extraction probability than the commonly believed space-charge-limited (SCL) sheath. Formation of the proposed electronegative inverse sheath and the SCL sheath near the H^--emitting surface is investigated by the continuum kinetic simulation. Dedicated theoretical analyses are also performed to characterize the electronegative inverse sheath properties, which qualitatively agree with the simulation results. We further propose that the transition between the two sheath modes can be realized by tuning the cold ion generation near the emissive boundary. The electronegative inverse sheath is always coupled with a plasma consisting of only hydrogen ions with approximately zero electron concentration, which is reminiscent of the ion–ion plasma reported in previous NBI experiments.

Keywords: neutral beam injection, negative ion source, negative ion extraction, plasma sheath

(Some figures may appear in colour only in the online journal)

* Authors to whom any correspondence should be addressed.

1. Introduction

Neutral beam injection (NBI) is crucial to provide sufficient heating and current drive for the operation of fusion devices [1–3]. An ion source is indispensable for the NBI system, and both positive and negative hydrogen ion sources have been developed for the NBI systems. Positive-ion-based NBI is commonly employed in most present-day fusion devices [4–6]. A negative ion source has been tested for NBI in JT-60U, JT-60SA, LHD [7–10], and a prototype of a negative ion source for ITER-NBI is being developed [11, 12]. For future fusion reactors requiring higher power levels, positive ions can become difficult to neutralize compared with negative ions, where the use of a negative ion source in the NBI system becomes more favorable. In the negative-ion-based source for NBI, the maximum delivered current density of surface-produced H^- is however limited by the space charge effect, where a space-charge-limited (SCL) sheath is assumed to be formed in front of the H^--emitting surface and reflects most of the generated H^- back to the surface [13, 14]. H^- passing the minimum potential well of the SCL sheath are strongly accelerated by the SCL sheath, and their extraction probability is reduced due to a larger gyroradius and longer transport path [15, 16]. The present work is thus motivated and aims to address this issue with an alternative sheath structure in the extraction region of a negative ion source.

In the negative hydrogen ion source, H^- are commonly produced on the plasma grid (PG) made of molybdenum or molybdenum-coated copper with a cesium deposit. Incoming positive hydrogen ions (H^+) and hydrogen atoms are converted to H^- at the PG surface. Generated H^- beams are then accelerated by the extraction voltage and neutralized before entering the fusion device. The surface-emitted H^-, however, undergo persistent collisions and can be destroyed by, e.g. two-body recombination, mutual neutralization, collision with electrons or hydrogen atoms, photodetachment, etc, before being extracted [17, 18]. Mitigating the H^- destruction is crucial to improve the negative ion source production rate.

The initial state of H^- when injected into plasma is essential to the H^- transport in the extraction region, which is regulated by the sheath near the PG. Sheath physics near the PG surface shares some similarities with those near the solid boundary emitting electron flux due to, e.g. secondary electron emission (SEE), thermionic emission, photoemission, etc. A local potential minimum near the emissive surface, called a virtual cathode (VC), was observed in numerous previous simulations for surfaces emitting both electrons and H^- [19–22]. The VC is always accompanied by an SCL sheath near the emissive surface, featuring a nonmonotonic sheath potential profile. Potential distribution between the potential minimum of the VC and the plasma is the same as in a classic Debye sheath coupled with a Bohm presheath. Recent theories and experiments questioned the stability of the SCL sheath if the sheath is collisional: positive ion charge-exchange collision in the VC should create cold ions that are trapped by local potential dip and gradually fill up the VC [23–26]. This eventually yields the so-called inverse sheath, where the wall potential floats above the plasma potential and the presheath potential profile is flat. Both the SCL sheath and inverse sheath have been observed experimentally for a range of plasma conditions [27–29]. When a sheath is inverted, negative particles (either electron or H^-) injected into plasma should contain zero drift velocity without sheath acceleration, as opposed to the SCL sheath. This inspires us to tailor the inverse sheath formation near the PG to improve the H^- extraction.

The paper is structured as follows. Section 2 introduces the employed simulation model. Section 3.1 illustrates and compares the inverse and SCL sheath near the PG with the adopted simulation model and expatiates their main differences. Section 3.2 develops the self-consistent electronegative inverse sheath theory, allowing for the estimation of inverse sheath parameters. Section 3.1 compares the theory and simulation results, and highlights the benefit of using inverse sheath mode to improve H^- extraction. Section 4 revisits previous NBI experiments which support the existence of the proposed inverse sheath, and provides instructions to measure the inverse sheath in practical NBI devices.

2. Simulation model

A 1D1V continuum kinetic simulation model is constructed to simulate the H^- extraction region in the negative ion source for NBI heating. A schematic of the considered extraction region and its location in a type of negative ion source are shown in figure 1. The left boundary of the simulation model is the PG surface in the direction facing the expansion region. Plasmas in the expansion region penetrate the filter magnetic field and arrive at the PG surface. The right boundary in figure 1(*a*) represents the wall of the ion source. The present work only focuses on the sheath formation in front of the PG facing the expansion region. This simulation model was also employed in a range of previous works investigating the sheath formation near the PG [13, 14, 24, 30, 31]. H^- generated at the PG surface move toward the bulk plasma, where no large electric field is present. They collide with the plasma particles and turn back toward the PG, until some of them reach the apertures and pass through the meniscus, entering the region where they are accelerated by the electric field. Note that the deflecting field is generated by permanent magnets to deflect electrons after H^- enter the meniscus, which should be located in the left of the PG in figure 1(*b*) (not shown in figure 1(*b*) for simplicity but can be found in, e.g. [15]). H^- are subject to Lorentz force and volumetric losses in the above processes, but these processes are not simulated by the present model. In reality, expansion-region plasmas come from the inductively coupled plasmas generated by the RF coils in the driver region in figure 1(*b*). Simulation in the present work is however not restricted to the RF-driven negative ion source and is applied to a variety of sources with similar extraction regions, e.g. H^- sources based on the filament-driven DC-arc discharge [32].

On the left boundary, H^- are emitted from the PG, which is usually made of molybdenum or molybdenum-coated copper. The PG is usually covered with cesium to increase the H^- production yield. The cesium-enhanced surface H^- emission process is simplified by setting a constant H^- flux density on

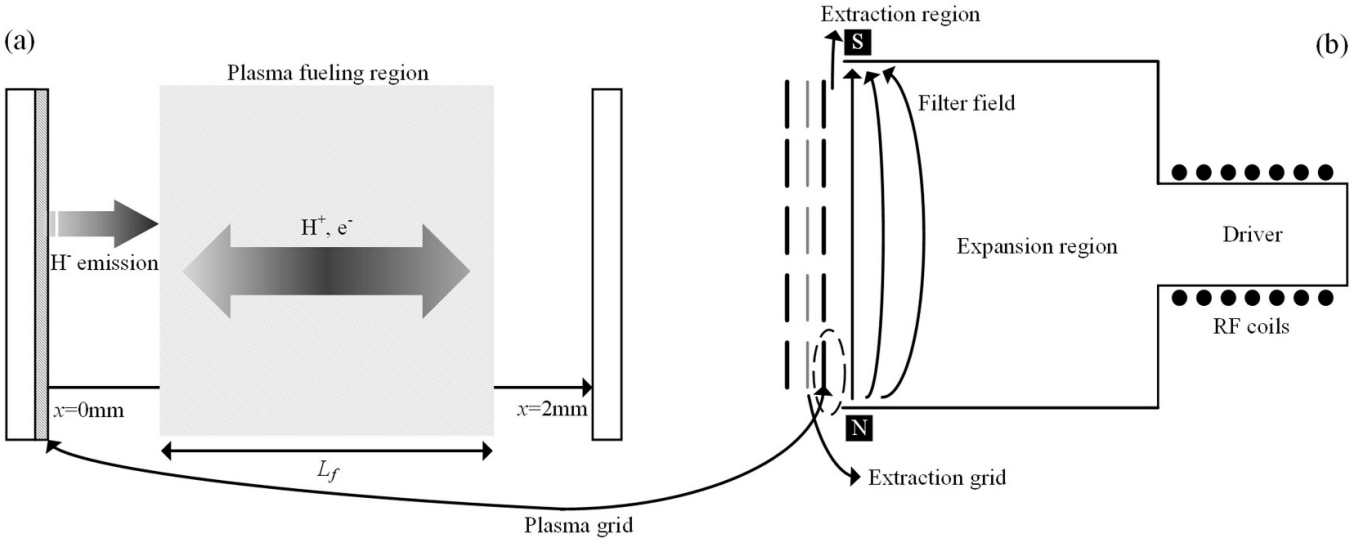

Figure 1. A schematic of (*a*) the simulated region and (*b*) the location of the simulated region in a type of negative ion source for NBI heating. The length of the plasma fueling region L_f is marked out. Note that the deflecting field lines in the left of the PG are not shown in (*b*) for simplicity. Here, (*a*) is a zoom-in of the region marked by the dashed circle in (*b*).

the left boundary, and the cesium species is neglected as the cesium concentration is usually more than one order of magnitude lower than the hydrogen [33]. The constant emission flux is commonly adopted for the sheath modeling near the PG surface [14, 24], corresponding to the surface H^- production due to incoming hydrogen atoms. This assumption will be further justified in section 3.2. A volumetric H^- source is not considered in the present simulation as the volumetric H^- production rate is shown to be significantly lower than the surface production [34].

The plasmafueling region, covering sixty percent of the entire simulation domain, represents the plasmas coming from the expansion region (shaded area in figure 1(*a*)), which generates electron–H^+ pairs with constant temperatures according to the boundary H^+ loss. The plasma fueling region here is specially designed to maintain the bulk plasma density at a desired level, in order to facilitate the comparison with theory and simulation parameter scans. In each time step, the H^+ flux toward both left and right boundaries ($\Gamma_{\mathrm{H+,L}}$ and $\Gamma_{\mathrm{H+,R}}$) are summed up, and the plasma fueling term is calculated as $S_\mathrm{charge} = \frac{\Gamma_{\mathrm{H+,L}}+\Gamma_{\mathrm{H+,R}}}{n_0 L_\mathrm{f}} f_{\mathrm{s}0}$. Here, n_0 is the desired bulk plasma density level, L_f is the length of the plasma fueling region, and $f_{\mathrm{s}0}$ is the electron or H^+ velocity distribution function (VDF) in equilibrium (to be given later). Because H^- are not intrinsically generated in bulk plasma but are supplied by the PG surface emission, the boundary loss of H^- is not compensated by the plasma fueling term. This choice of fueling region is widely used in pertinent sheath modeling [21, 23].

The code simulates the evolution of the following kinetic equations for the three plasma species H^-, H^+, and electrons [35]

$$\frac{\partial f_{\mathrm{H-}}(x,v_{\mathrm{H-}})}{\partial t} = -v_{\mathrm{H-}}\frac{\partial f_{\mathrm{H-}}(x,v_{\mathrm{H-}})}{\partial x} - \frac{q_{\mathrm{H-}}E(x)}{m_\mathrm{H}}\frac{\partial f_{\mathrm{H-}}(x,v_{\mathrm{H-}})}{\partial v_{\mathrm{H-}}} \tag{1}$$

$$\frac{\partial f_{\mathrm{H+}}(x,v_{\mathrm{H+}})}{\partial t} = -v_{\mathrm{H+}}\frac{\partial f_{\mathrm{H+}}(x,v_{\mathrm{H+}})}{\partial x} - \frac{q_{\mathrm{H+}}E(x)}{m_\mathrm{H}}\frac{\partial f_{\mathrm{H+}}(x,v_{\mathrm{H+}})}{\partial v_{\mathrm{H+}}} + \frac{\Gamma_{\mathrm{H+,tot}}}{n_0 L_\mathrm{f}} f_{\mathrm{H+0}}\Big|_\mathrm{pf} + S_{\mathrm{H+,CX}} \tag{2}$$

$$\frac{\partial f_\mathrm{e}(x,v_\mathrm{e})}{\partial t} = -v_\mathrm{e}\frac{\partial f_\mathrm{e}(x,v_\mathrm{e})}{\partial x} - \frac{q_\mathrm{e}E(x)}{m_\mathrm{e}}\frac{\partial f_\mathrm{e}(x,v_\mathrm{e})}{\partial v_\mathrm{e}} + \frac{\Gamma_{\mathrm{H+,tot}}}{n_0 L_\mathrm{f}} f_{\mathrm{e}0}\Big|_\mathrm{pf} + S_{\mathrm{e,e-n}}. \tag{3}$$

Here, f_s is the VDF of the species, with the subscript 's' representing 'H^-', 'H^+', and 'e'. Meanwhile, v_s is the species velocity, q_s is the species charge, 'pf' represents the plasma fueling region, E is the electric field, and $\Gamma_{\mathrm{H+,tot}}$ is the total H^+ flux at both boundaries to calculate the electron and H^+ fueling rate. Note that the present simulation does not consider the molecular hydrogen ion species (H_2^+, H_3^+), which can contribute to the H^- volumetric losses. The H^- volumetric losses are not crucial for the sheath formation near the PG surface, but significantly affect the H^- transport to the extraction grid (not simulated). Therefore, in previous works studying PG sheath physics, the molecular ions are usually not considered for simplicity [24, 30]. The salient characteristics of the involved sheath physics in the present work are not expected to be strongly affected by the molecular ions. The effects of molecular ions will be studied with the planned 2D particle-in-cell (PIC) simulation code of the entire extraction region and are not further discussed in the following sections. The kinetic equations contain the time derivative, two advections, and the collision terms. The electric field is solved from the following Poisson equation:

$$\frac{\partial^2\varphi}{\partial x^2} = -\frac{e}{\varepsilon_0}\left(n_{\mathrm{H+}} - n_{\mathrm{H-}} - n_{\mathrm{e-}}\right). \tag{4}$$

Here, φ is the space potential, ε_0 is the vacuum permittivity, and n_s are densities of species. Note that both left and right

Table 1. Boundary conditions for VDFs of three plasma species.

Boundary	H^+	H^-	Electron
Left ($x=0$)	$f_{H+}\|_{x=0,v_{H+}>0}=0$	$f_{H-}\|_{x=0,v_{H-}>0}=\frac{m_H}{T_{H-}}\Gamma_{H-}\exp\left(-\frac{m_H v_{H-}^2}{2T_{H-}}\right)$	$f_e\|_{x=0,v_e>0}=0$
Right ($x=L$)	$f_{H+}\|_{x=L,v_{H+}<0}=0$	$f_{H-}\|_{x=L,v_{H-}<0}=0$	$f_e\|_{x=L,v_e<0}=0$

boundaries have zero potential. In reality, the PG can be biased to help improve the H^- extraction. The bias voltage should affect the size and potential of the sheath, which regulate the flux balance and plasma density profiles. At the moment, the influence of bias voltage is not considered, but it will be investigated in our future works.

The plasma fueling terms of H^+ and electrons are only given in the plasma fueling region, where $\Gamma_{H+,tot}$ is the sum of total ion flux at both boundaries, n_0 is the desired plasma density, L_f is the length of the plasma fueling region, and f_{s0} is the Maxwellian distribution of species as follows:

$$f_{s0}(x,v_s)=n_0\sqrt{\frac{m_s}{2\pi T_s}}\exp\left(-\frac{m_s v_s^2}{2T_s}\right). \tag{5}$$

Here, T_s is the species temperature. The terms $S_{H+,CX}$ and $S_{e,e-n}$ characterize the H^+ charge-exchange collision and electron thermalization due to electron–neutral collisions. Both collision operators remove a portion of the VDF at a rate that is inversely proportional to the collision mean free path. Here, $S_{H+,CX}$ replaces the ion VDF with a cold ion of temperature T_{H0} of the neutral hydrogen, and $S_{e,e-n}$ replaces the electron VDF with an electron of temperature T_e. The expressions of the two Bhatnagar–Gross–Krook (BGK) collision operators are shown below [36]:

$$S_{H+,CX}=-\frac{|v_{H+}|}{\lambda_{CX}}f_{H+}+\frac{f_{H0}}{n_0\lambda_{CX}}\int_{-v_{H+,lim}}^{v_{H+,lim}}|v_{H+}|f_{H+}(x,v_{H+})\,dv_{H+} \tag{6}$$

$$S_{e,e-n}=\nu_{en}\left[\frac{n_e(x)}{n_0}f_{e0}-f_e(x,v_e)\right]. \tag{7}$$

Here, λ_{CX} is the H^+ charge-exchange collision mean free paths, $v_{H+,lim}$ is the velocity limit of the simulation, and ν_{en} is the electron thermalization rate that characterizes the electron–neutral collision. The treatment of electron–neutral collision is simplified. Equation (7) only aims to thermalize electrons such that the electron VDF approaches Maxwellian at a given rate. The present simulation results with an inverse sheath formed in front of the PG are shown not to be sensitive to the electron–neutral collision rate, when an ion–ion plasma is achieved with very low plasma electron concentration. H^- collision barely affects the simulation results. Also, its collision mean free path is large compared with the gap distance; hence, H^- collisions are neglected. H^- collisions are more obvious when being transported to the extraction grid (not simulated), where the gyration under the filter magnetic field makes their trajectories significantly longer. The same treatment was adopted in a PIC simulation model of similar plasma conditions [24].

The initial plasma conditions are a uniform Maxwellian distribution, as shown in equation (5) in the plasma fueling region for H^+ and electrons, and without H^- everywhere. The boundary conditions for H^+ and electrons are to set the plasma-facing side of the VDF at the wall as zero, since the particle reflection and surface electron emission are not considered. The H^- surface emission flux Γ_{H-} is implemented in the left wall H^- VDF and the right boundary is perfectly absorbing for H^-. The Γ_{H-} can be set as a given constant or can be determined by the background neutral pressure. All the VDF boundary conditions are listed in table 1.

The detailed simulation parameters are as follows: hydrogen ions, neutral and electron temperatures are $T_{H+}=0.8$ eV, $T_{H-}=0.8$ eV, $T_{H0}=0.026$ eV (300 K), $T_e=2$ eV. The plasma density is $n_0=10^{17}\mathrm{m}^{-3}$. The choices of plasma density and temperature are based on previous simulation of the extraction region [30]. Note that the neutral hydrogen temperature can be higher for practical sources and is as high as 2000–3000 K. The simulation results are however not very sensitive to T_{H0} and a discrepancy of 5% for the sheath potential is observed when increasing the T_{H0} from 300 K up to 3481 K. The electron thermalization rate $\nu_{en}=kv_{e,Th}/L$, where k is an adjustable factor and $v_{e,Th}$ is the electron thermal velocity. The simulation results are not sensitive to k and a value of 1 is chosen. The mean free path for the ion charge-exchange collision λ_{CX} is varied to achieve the sheath mode transition (to be discussed later in section 3.3.) Here, $\lambda_{CX}=0.02$ m is chosen if not specified, corresponding to a background neutral pressure of approximately 0.3 Pa, which is the typical working pressure in the extraction region. Surface H^- flux can be a given constant or can be proportional to the background pressure with a given production yield, to be discussed in section 3.2. By default, a constant H^- emission flux of 2×10^{21} $\mathrm{m}^{-2}\mathrm{s}^{-1}$ is provided, corresponding to an emission current of approximately 320 Am^{-2}. The simulation gap $L=2$ mm, and the plasma fueling region length $L_f=1.2$ mm, located between 0.4 mm $\leqslant x\leqslant$ 1.6 mm. The choice of gap distance is the same as in [37]. The spatial resolution is $\Delta x=5\times10^{-6}$m, and the time step $\Delta t=5\times10^{-13}$ s. The velocity range is eight times the electron thermal velocity for electrons, and 40 times the ion thermal velocity for all ions, divided into 400 points. The choices of phase space and time resolution are dictated by the Courant–Friedrichs–Lewy conditions, and the selected velocity range must be sufficiently wide to avoid not covering the high-velocity tails of the VDFs. Convergence is achieved when key plasma parameters, including the sheath potential, boundary plasma flux, and mean plasma density, all have variations below 0.1% for a duration of $10^4\Delta t$. The above choices of simulation parameters are based on previous modeling and measurement of the extraction region in the negative ion source of similar working conditions [14, 24, 30, 38].

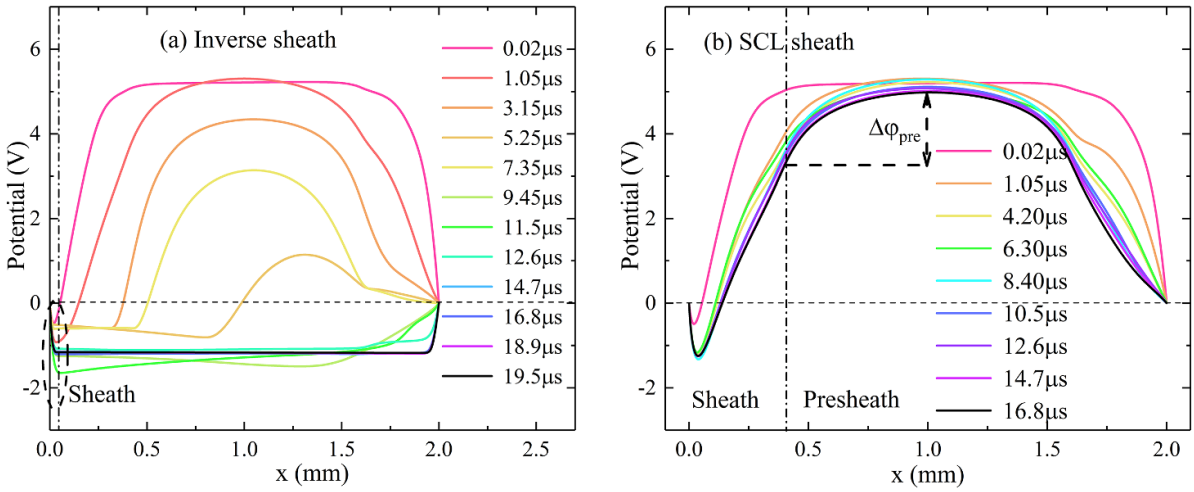

Figure 2. Space potential evolution in the formation of an electronegative (*a*) inverse sheath and (*b*) SCL sheath. All the simulation conditions are the same, except that the H^+ charge-exchange collision mean free path is 0.02 m for (*a*) and 0.1 m for (*b*). For the converged potential curves (black), the presheath potential drop $\Delta\varphi_{\mathrm{pre}}$ is marked out, the sheath-edge locations are marked by the dash–dotted lines, and the sheath and presheath regions are indicated.

3. Simulation results and theoretical model

3.1. Simulation of the electronegative inverse sheath and SCL sheath

The characteristics of the electronegative inverse sheath are compared with the SCL sheath using the simulation model presented in section 2. The two simulation cases have the same input parameters, except that the H^+ charge-exchange collision mean free path is different. The inverse sheath case uses the default mean free path of 0.02 m, as shown in section 2, derived from the nominal working pressure of 0.3 Pa. The SCL sheath case uses 0.1 m as the mean free path, which corresponds to a lower working pressure to reproduce the SCL sheath in front of the PG. The following analyses will show that under the given plasma conditions, it should be the electronegative inverse sheath that will be formed in reality. The time evolution of space potential distribution during the formation of an inverse/SCL sheath is shown in figure 2. The potential dip near the left emissive boundary is only visible in the beginning of the inverse sheath run, which is then destroyed by cold H^+ generated by the charge-exchange collision, eventually leaving a negative bulk plasma potential relative to the boundary. A flat potential profile is found in the entire space, except near the two boundaries, indicating no presheath structure predicted by the Bohm criterion. Here, the H^+ ions should satisfy the Maxwellian distribution with no significant temperature gradient. For the SCL sheath case, a stable potential dip (VC) is maintained, and the sheath remains a classic Debye sheath between the bottom of the potential dip and the bulk plasma, accompanied by a clear Bohm presheath potential drop, marked in figure 2(*b*). The obtained SCL sheath structure in front of the PG surface is consistent with previous simulation works [13, 30]. Note that both the H^- density in bulk plasma and the H^- surface emission affect the Bohm presheath potential drop according to previous theories, which deviates the H^+ energy at the sheath edge away from $0.5T_e$ [14].

The plasma density distributions of the converged runs for the electronegative inverse and SCL sheath are shown in figure 3. With an inverse sheath formed, the electron density drops to a very low level ($\sim 10^{12}$ m^{-3}) and the entire plasma is formed only by H^+ and H^-. The H^- density peaks at the emissive boundary due to the sum of emitted H^- and H^- reflected by the inverse sheath, with the H^+ density quickly decaying in the inverse sheath toward the left boundary. The H^+ fluxes at the left boundary and right boundary are 8.4×10^{19} m^{-2} s^{-1} and 8.5×10^{19} m^{-2} s^{-1}, which are not very different due to near-symmetrical sheath potential distribution. The H^- flux at the left boundary is 2.1×10^{21} m^{-2} s^{-1}, which is much larger than the right boundary H^- flux of 8.5×10^{19} m^{-2} s^{-1} due to the contribution of H^- reflected by the inverse sheath. Electron fluxes at both boundaries are more than four orders of magnitudes lower than the H^+ fluxes and are negligible. Although an inverse-like sheath potential is also formed on the right grounded boundary (figure 2(*a*)), both the H^+ and H^- densities decrease when approaching the boundary, and the H^- density drops slower than H^+ to keep the current balance. When an SCL sheath is formed at the left emissive boundary, the electron density is above the H^- density in bulk plasma. The net space charge density is negative near the PG surface, and becomes positive when crossing the minimum potential of the VC toward the bulk plasma, consistent with previous SCL theories and simulations. This transition from net negative to net positive space charge in the SCL sheath is also called a double layer, which is shown in figure 3(*b*) [13, 30]. The density distribution in bulk plasma and the presheath is similar to that of classic electronegative plasma.

The H^- behavior when entering the plasma from the sheath, which is critical for their extraction, is fundamentally different in the electronegative inverse sheath and SCL sheath. In the SCL sheath, negative ions that penetrate the VC sheath barrier are strongly accelerated and carry energy of several

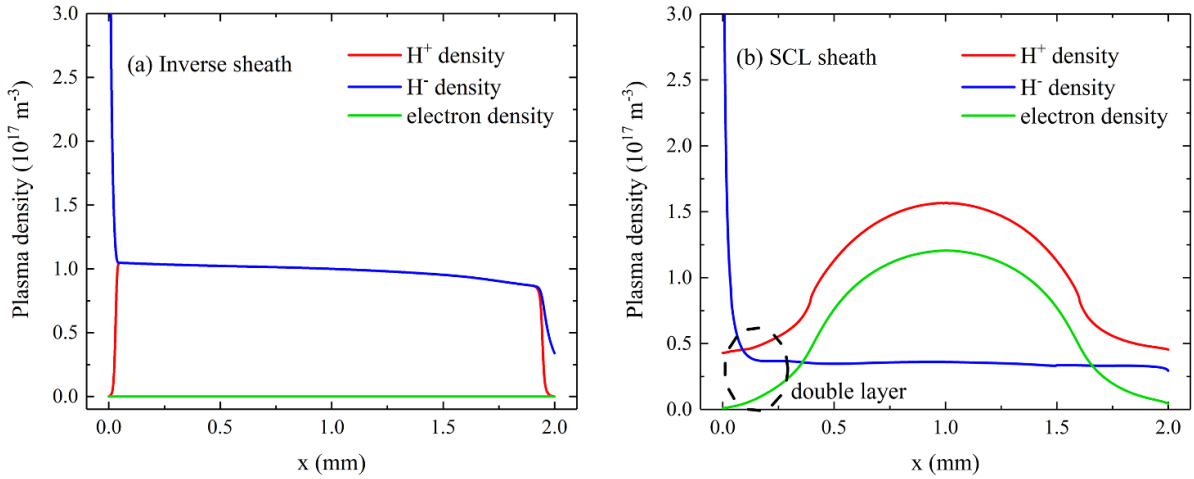

Figure 3. Plasma density distribution for converged simulations of an electronegative (*a*) inverse sheath and (*b*) an SCL sheath. All the simulation conditions are the same, except that the H^+ charge-exchange collision mean free path is 0.02 m for (*a*) and 0.1m for (*b*).

times the electron temperature, whereas H^- should have zero drift velocity when entering plasma from the inverse sheath, whose mean velocity is comparable with the ion thermal velocity. A comparison of the normalized H^- VDF at the sheath edge for the two types of sheath is shown in figure 4. The VDF of the inverse sheath is concentrated near $v_{H-} = 0$, and the VDF in the SCL sheath features a high velocity peak around 3×10^4 ms^{-1} due to sheath acceleration of H^- from the surface, corresponding to an energy of approximately 4.6 eV, which is consistent with figure 2(*b*). The lower part of the H^- VDF in the SCL sheath consists of H^- reflected by the sheath barrier ($v_{H-} < 0$), H^- penetrating the inverse sheath barrier ($v_{H-} > 0$), and the H^- coming from bulk plasma ($v_{H-} < 0$). The starting energy or entering energy of H^- at the sheath entrance in the SCL sheath is hence much larger than that in the inverse sheath. Detailed quantitative analyses will be given combined with dedicated theoretical analyses in section 3.2. The sheath entrance, or sheath edge, is the interface connecting the presheath and sheath region. In the present simulation, the sheath edge is defined as the closest position to the midplane with net charge greater than 1% of the H^+ density for the SCL sheath. This definition is easier to implement in the simulation than the Bohm criterion, and similar approaches are adopted in a range of related simulations [39–41]. For the inverse sheath, the edge is simply defined as the outmost position with a zero potential gradient, since the inverse sheath has a flat potential in the presheath region. It can also be stated that the inverse sheath is not coupled to a presheath. The sheath-edge locations, sheath, and presheath regions are marked out in figure 2.

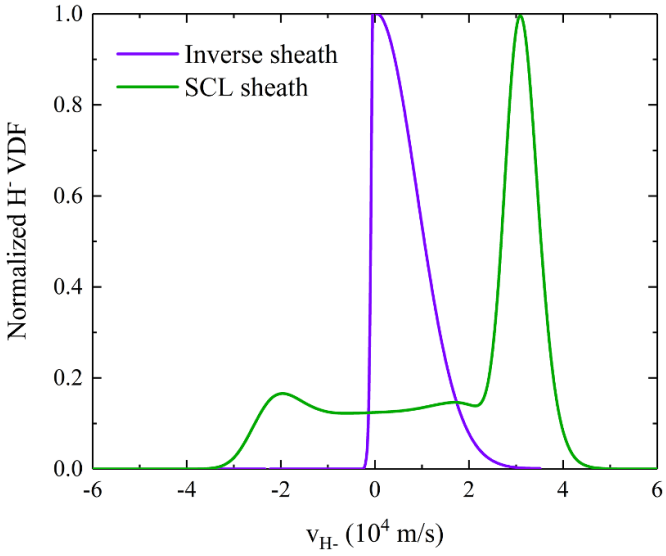

Figure 4. A comparison of the H^- VDF at the sheath edge for the electronegative inverse sheath and SCL sheath. H^- are strongly accelerated by the SCL sheath, while the inverse sheath has no sheath acceleration.

3.2. Theoretical ground

In this section, the theoretical ground of the electronegative inverse sheath will be established to compare with the simulation results. The plasma flow in the electronegative inverse sheath is shown in figure 5, including H^+ flux from plasma (indexed '*i*'), H^+ flux reflected by the inverse sheath (indexed '*i, ref*'), surface-emitted H^- flux (indexed negative ion beam, '*nb*'), H^- flux reflected by the inverse sheath (indexed as '*nb, ref*'), and H^- flux from plasma (indexed as '*np*'). The potential at the sheath entrance is zero, and the inverse sheath potential is equal to the wall potential φ_w.

The sheath potential will be solved by combining the charge neutrality at the sheath edge, the flux balance at the wall, and the expression of the surface H^- emission flux. At the sheath edge, H^+ density consisting of H^+ from plasma and those reflected by the sheath, is equal to the total H^- density:

$$n_{\mathrm{i}}^{\mathrm{se}} + n_{\mathrm{i,ref}}^{\mathrm{se}} = n_{\mathrm{nb}}^{\mathrm{se}} + n_{\mathrm{np}}^{\mathrm{se}}. \tag{8}$$

Here, the subscript 'se' represents the sheath edge. Note that $n_{\mathrm{nb,ref}}^{\mathrm{se}} = 0$ at the sheath edge. Reflected H^+ density is obtained by integrating a truncated H^+ VDF, $n_{\mathrm{i,ref}} = n_{\mathrm{i}}^{\mathrm{se}} \mathrm{erf}(\sqrt{\frac{e(\varphi_w - \varphi)}{T_i}})$, and the surface-emitted beam

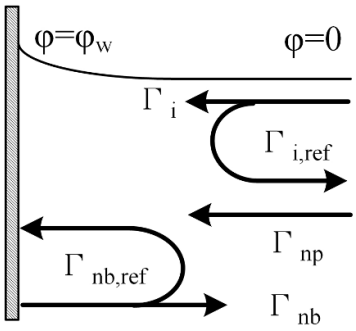

Figure 5. A schematic of the plasma flow and sheath potential profile in an electronegative inverse sheath.

H^- density follows the Boltzmann distribution, $n_{nb} = n_{nb}^{w}\exp(\frac{e(\varphi-\varphi_w)}{T_i})$, as the electric field force is balanced by the pressure gradient force. Here, the subscript 'w' represents the wall. Equation (8) is then rewritten as follows, assuming the plasma density at the sheath entrance n_0:

$$n_i^{se}\left[1+\mathrm{erf}\left(\sqrt{\frac{e\varphi_w}{T_i}}\right)\right] = n_{nb}^{w}\exp\left(-\frac{e\varphi_w}{T_i}\right) + n_{np}^{se} = n_0. \quad (9)$$

In addition, the net plasma fluxes at the wall must be zero to guarantee the current balance, which includes H^+ flux Γ_i, surface-emitted H^- flux Γ_{nb}, reflected H^- flux $\Gamma_{nb,ref}$, and H^- flux from plasma Γ_{np}:

$$\Gamma_i^{w} = \Gamma_{np}^{w} + \Gamma_{nb,ref}^{w} - \Gamma_{nb}^{w}. \quad (10)$$

The wall H^+ flux is equal to $\Gamma_i^{w} = \Gamma_i^{se}\exp(-\frac{e\varphi_w}{T_i})$, and the wall reflected H^- flux is proportional to the surface emission flux, $\Gamma_{nb,ref}^{w} = \Gamma_{nb}^{w}[1-\exp(-\frac{e\varphi_w}{T_i})]$. The H^- flux from plasma is conserved in the sheath region and is expressed by its sheath-edge density, $\Gamma_{np} = n_{np}^{se}\sqrt{\frac{2T_i}{\pi m_i}}$. The surface-emitted H^- flux is expressed as $\Gamma_{nb}^{w} = n_{nb}^{w}\sqrt{\frac{2T_i}{\pi m_i}}$, assuming half-Maxwellian distribution for the surface-emitted H^- ions. Equation (10) is then rewritten as:

$$n_i^{se}\exp\left(-\frac{e\varphi_w}{T_i}\right) = n_{np}^{se} - n_{nb}^{w}\exp\left(-\frac{e\varphi_w}{T_i}\right). \quad (11)$$

Meanwhile, the surface-emitted H^- flux is produced by the surface processes due to incoming H^+ and neutral hydrogen atoms, with the emission yield Y_+ and Y_{H0}, which gives the following emission flux:

$$\Gamma_{nb}^{w} = Y_+\Gamma_i^{w} + Y_{H0}\Gamma_{H0}^{w}. \quad (12)$$

The wall hydrogen atom flux Γ_{H0}^{w} is proportional to the background neutral pressure p_{H0}; here, an effective density $n_{H,eff}$ is introduced to facilitate the derivation. This effective density is defined as $Y_{H0}\Gamma_{H0}^{w} = n_{H,eff}\sqrt{\frac{2T_i}{\pi m_i}}$, and is equal to:

$$n_{H,eff} = Y_{H0}p_{H0}/\sqrt{T_{H0}T_i}. \quad (13)$$

Here, T_{H0} is the neutral hydrogen temperature. Combining equations (12) and (13), the following equation of wall-emitted H^- density is derived as:

$$n_{nb}^{w} = Y_+ n_i^{se}\exp\left(-\frac{e\varphi_w}{T_i}\right) + n_{H,eff}. \quad (14)$$

Combining equations (9), (11), and (14), an equation containing only the variable φ_w is obtained:

$$Y_+\exp\left(-\frac{e\varphi_w}{T_i}\right) + 0.5 = \left[1+\mathrm{erf}\left(\sqrt{\frac{e\varphi_w}{T_i}}\right)\right] \times \left[0.5\exp\left(\frac{e\varphi_w}{T_i}\right) - \frac{n_{H,eff}}{n_0}\right]. \quad (15)$$

Solving equation (15) numerically provides the inverse sheath potential as a function of the neutral pressure p_{H0}, production yield Y_+ and Y_{H0}, and the plasma density n_0. The following discussions will further simplify the sheath potential calculation by adding supplementary assumptions.

In the simulation presented in section 3.1, the surface-emitted H^- flux is constant, which is based on the assumptions that H^- production is mainly contributed by neutral hydrogen due to a low degree of ionization, and that the neutral pressure is uniform and stays at a constant level. For the parameters chosen in the simulation, the wall hydrogen neutral flux is approximately 20 times larger than the H^+ flux, considering a 1% ionization degree, 0.8 eV ion temperature, and 0.026 eV neutral temperature. Note that the production yields Y_+ and Y_{H0} chosen here are based on the existing theory predictions and measurements [42–44]. It is therefore possible to discard the $Y_+\Gamma_i^{w}$ term in equation (12), and equations (9), (11), and (14) can be solved with an additional term defined as $\gamma_{H-} = \frac{\Gamma_{nb}^{w}}{\Gamma_{np}}$, which is the ratio of surface-emitted H^- flux over the incoming H^- flux from plasma at the wall. The term γ_{H-} resembles the SEE coefficient from a solid boundary but characterizes fundamentally different physics, since emitted H^- is not directly created by incident H^-, as in SEE. Solving for the inverse sheath with γ_{H-} leads to the following equation:

$$\frac{e\varphi_w}{T_i} = \ln(\gamma_{H-}) + \ln\left[\frac{1+\exp\left(-\frac{e\varphi_w}{T_i}\right)/\left(1+\mathrm{erf}\left(\sqrt{\frac{e\varphi_w}{T_i}}\right)\right)}{1-\exp\left(-\frac{e\varphi_w}{T_i}\right)/\left(1+\mathrm{erf}\left(\sqrt{\frac{e\varphi_w}{T_i}}\right)\right)}\right]. \quad (16)$$

For a constant H^- emission flux Γ_{nb}^{w}, the ratio γ_{H-} is equal to:

$$\gamma_{H-} = \frac{\Gamma_{nb}^{w}}{n_0\sqrt{\frac{2T_i}{\pi m_i}}} \Bigg/ \left[1 - \frac{\Gamma_{nb}^{w}}{n_0\sqrt{\frac{2T_i}{\pi m_i}}}\exp\left(-\frac{e\varphi_w}{T_i}\right)\right]. \quad (17)$$

Equations (16) and (17) solve for the sheath potential using the surface emission flux Γ_{nb}^{w} dictated by the neutral pressure p_{H0} and the production yield Y_{H0}, in addition to the plasma density n_0.

An analytical expression for the inverse sheath potential can be derived if, in addition, the positive ions are ignored in the inverse sheath. This somewhat bold assumption characterizes a limiting condition with high inverse sheath potential, such

that most H^+ are immediately reflected back to the plasma by the inverse sheath barrier, analogous to the neglected electron density in a high-voltage Debye sheath, described by, e.g. the Child–Langmuir law. With the above assumption, equations (16) and (17) are rewritten as:

$$\frac{e\varphi_{\rm w}}{T_{\rm i}} = \ln\left(\gamma_{\rm H-}\right) \tag{18}$$

$$\gamma_{\rm H-} = \frac{2\Gamma_{\rm nb}^{\rm w}}{n_0\sqrt{\frac{2T_{\rm i}}{\pi m_{\rm i}}}}. \tag{19}$$

The limiting condition of equations (18) and (19) clearly shows that the inverse sheath potential increases monotonically with the surface emission flux. Note that the sheath potential given by equations (18) and (19) is more accurate with large surface emission fluxes, such that the H^+ density is sufficiently low in the inverse sheath. A scan of the surface emission flux is performed, and the inverse sheath potential is calculated by equations (18) and (16), and equation (15) with a range of Y_+ values, shown in figure 6. The choices of H^- emission yield are based on previous simulations and measurements [30, 45]. The logarithmic increase of $\varphi_{\rm w}$ with surface emission flux, predicted by equation (18), somewhat underestimates $\varphi_{\rm w}$ compared with the other two methods considering H^+ in the sheath. Sheath potentials calculated by equations (16) and (15) are identical when $Y_+ = 0$, and are approximately the same unless Y_+ is more than four times larger than Y_{H0}. Since this unphysically large Y_+ value cannot be achieved in typical plasma conditions of the negative ion source, assuming constant surface H^- emission at a given pressure level should, in general, provide reasonably accurate predictions. Comparison of the theory predictions and simulation results will be given in section 3.3.

3.3. Theory validation and beneficial H^- starting energy for extraction

In this section, the theoretical predictions in section 3.2 are compared with the simulation results, for both an electronegative inverse and an SCL sheath, to highlight the benefit of using an inverse sheath to improve the H^- extraction efficiency. A scan of the H^- surface emission current is performed, and the corresponding inverse sheath potential and space potential profiles are shown in figure 7. The theory predictions slightly overestimate the inverse sheath potential, which is more obvious at low emission-current levels. The qualitative trend of the inverse sheath potential increasing with the emission current is in good agreement with the simulation results, see figure 7(*a*). The size of the inverse sheath remains approximately unchanged based on figure 7(*b*). The source of discrepancies mainly lies in the non-Maxwellian ion VDFs in the simulation due to the lack of sufficient collisionality. The assumption of zero H^+ density in the sheath is also less valid with the low emission current, which is why the discrepancies decrease with a higher emission current (i.e. higher sheath potential and lower ion density).

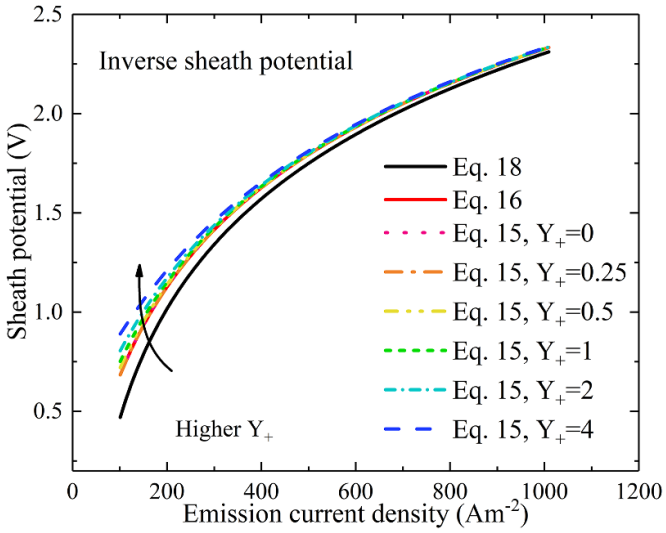

Figure 6. The inverse sheath potential calculated by equations (18) and (16), and equation (15) with different Y_+ values. Plasma density $n_0 = 10^{17}\rm m^3$, ion temperature $T_{\rm i} = 0.8$ eV, production yield $Y_{\rm H0} = 0.25$. Note that equation (15) with $Y_+ = 0$ gives identical results to equation (16).

A similar emission-current scan is also performed with a higher H^+ charge-exchange collision mean free path, as in section 3.1, where a stable electronegative SCL sheath appears, shown in figure 8. The simulation and theory achieve good consistency. The theoretical predictions are obtained using the well-known classic electronegative SCL sheath theory [14], and only the potential difference between the left boundary and the potential minimum at the VC is calculated, shortened to the SCL sheath barrier potential in the following discussions. This is because the sheath barrier $\varphi_{\rm scl}$ dictates the maximum H^- current that can be injected into bulk plasma, $J_{\rm inj,SCL}$, which is a key factor used to estimate the H^- extraction performance. Here, $J_{\rm inj,SCL}$ is calculated according to:

$$J_{\rm inj,SCL} = J_{\rm em}\exp\left(-\frac{e\varphi_{\rm scl}}{T_{\rm H-}}\right). \tag{20}$$

Here, $J_{\rm em}$ is the surface H^- emission current. The maximum injected current is expressed as $J_{\rm inj,SCL} = J_c j_b$, where j_b is a normalized term, as follows [14]:

$$j_b = \frac{1}{(2\eta_c)^2}\left\{2\nu_{\rm i}\eta_0\left[\sqrt{1+\frac{\eta_c}{\eta_0}}-1\right]+\exp\left(-\eta_c\right)\right.$$
$$\left.-1+\frac{\nu_n}{\gamma_T}\left[\exp\left(-\gamma_T\eta_c\right)-1\right]\right\}. \tag{21}$$

Here, η_c is the sheath-edge potential normalized by $T_{\rm e}$, $\nu_n = \frac{n_{\rm H-,se}}{n_{\rm e,se}}$, where the subscript 'se' is the location of the sheath edge, $\gamma_T = \frac{T_{\rm e}}{T_{\rm H-}}$, $J_c = en_{\rm e,se}\sqrt{\frac{T_{\rm e}}{m_{\rm H}}}(2\eta_c)^{2/3}$, $\nu_{\rm i} = 1 + 2\eta_c j_b + \nu_n$, and $\eta_0 = \frac{\nu_{\rm i}}{2(1-j_b+\gamma_T\nu_n)}$. The calculation of $\varphi_{\rm scl}$ requires the value of ν_n, which changes with the surface H^- emission flux and can only be determined combined with the simulation results;

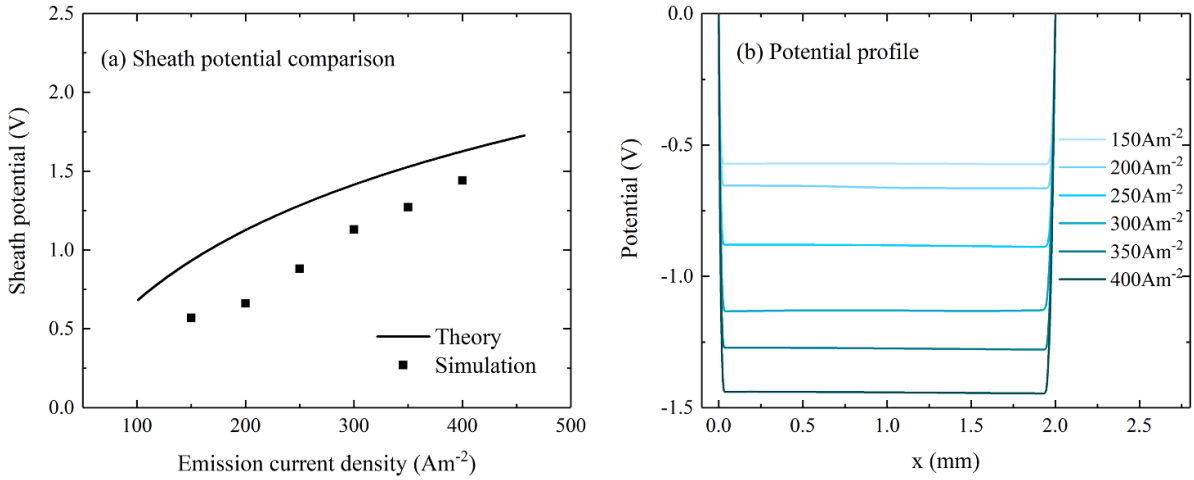

Figure 7. (*a*) The electronegative inverse sheath potential (positive value) given by theory and simulation, and (*b*) the simulated space potential distribution for various surface H^- emission currents when simulations converge. The theory prediction curve is calculated by equation (16).

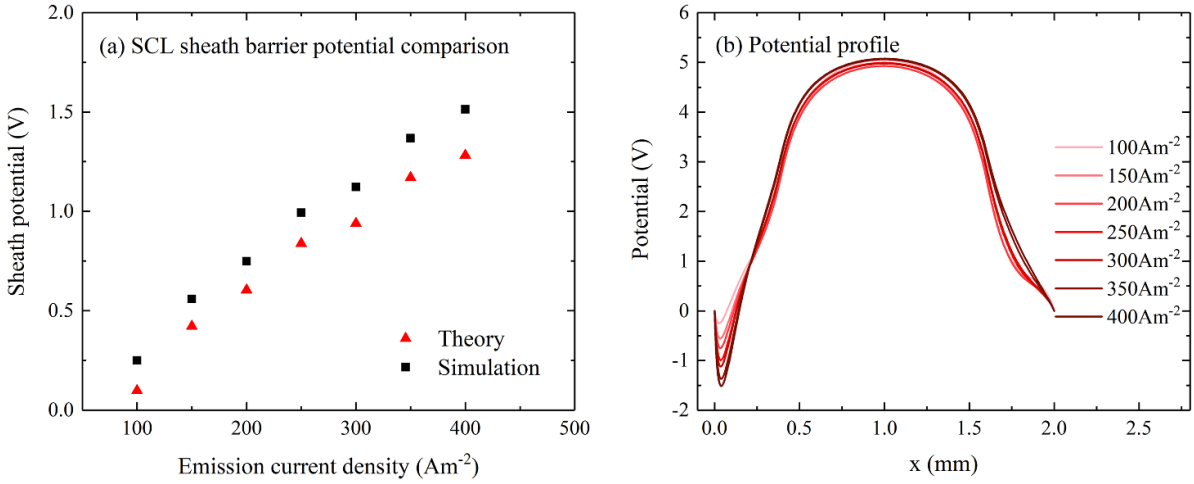

Figure 8. (*a*) The electronegative SCL sheath potential given by theory and simulation, and (*b*) the space potential distribution for various surface H^- emission currents. Theory points are calculated using existing classic SCL sheath theories.

hence, the theory predictions in figure 8 are discrete points in accordance with the simulation results. In previous theoretical analyses, ν_n is usually a given constant [13, 14].

The performance of the H^- extraction is primarily evaluated by the maximum amount of injected H^-, characterized by the H^- current at the sheath entrance, and the H^- extraction probability (or extraction efficiency). The following analyses will compare the pros and cons of using an electronegative inverse sheath or SCL sheath near the PG by focusing on the above two criteria, in order to determine the optimal H^- extraction solution.

The H^- created and injected from the PG surface are subject to the sheath barrier for both the inverse sheath and the SCL sheath. The maximum injected current at the sheath edge is $J_{\mathrm{inj,inv}} = J_{\mathrm{em}}\exp(-\frac{e\varphi_{\mathrm{inv}}}{T_{\mathrm{H-}}})$ for the inverse sheath and $J_{\mathrm{inj,SCL}} = J_{\mathrm{em}}\exp(-\frac{e\varphi_{\mathrm{scl}}}{T_{\mathrm{H-}}})$ for the SCL sheath, where J_{em} is the surface emission current. Here, $J_{\mathrm{inj,inv}}$ is given by the inverse sheath potential formulae derived in section 3.2. Taking the simplified solution of equations (18) and (19), the maximum injected H^- current for the inverse sheath is:

$$J_{\mathrm{inj,inv}} = 0.5 n_0 \sqrt{\frac{2T_{\mathrm{H-}}}{\pi m_{\mathrm{H}}}}. \tag{22}$$

The $J_{\mathrm{inj,SCL}}$ is prescribed by equations (20) and (21). Here, the variable ν_n is scanned with several γ_T values, while keeping $T_{\mathrm{H-}}$ and all the other parameters the same as the simulation setup. The calculation results are shown in figure 9. The maximum injected current is not very sensitive to ν_n (approximately 0.5–0.8 in simulations), but varies remarkably with the γ_T (T_e). Here, $\gamma_T = 2.5$ in the default simulation setup, where the SCL sheath should correspond to a larger injected current than the inverse sheath. When $\gamma_T = 5$ ($T_e = 4$ eV), the inverse sheath features a larger injected current for most ν_n than the SCL sheath. The observed trends are not sensitive to

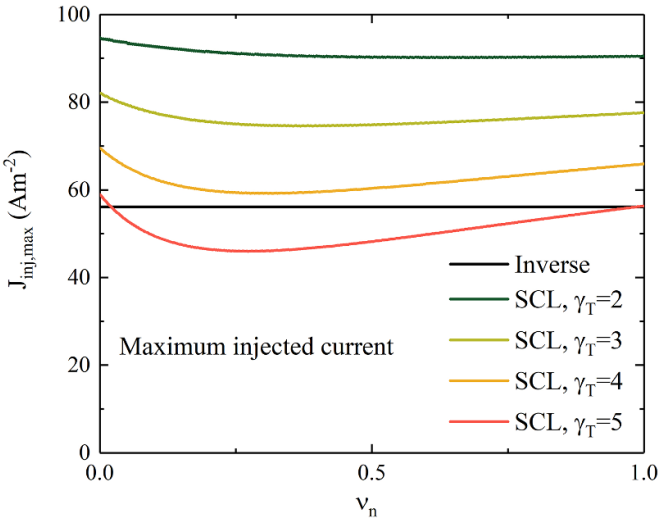

Figure 9. The maximum injected H^- current into the plasma for an inverse sheath and SCL sheath with different ν_n, γ_T values.

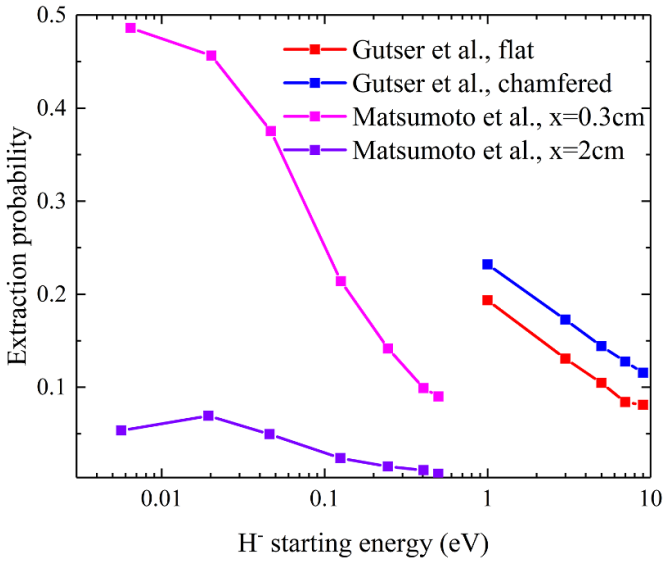

Figure 10. The influence of the H^- starting energy on the extraction probability from previous modeling works [15, 46]. The decrease in the extraction probability with the H^- starting energy is valid for different converter shapes (flat and chamfered) and varied radial positions from the chamber central axis (0.3 cm, 2 cm).

the plasma density (not shown). The above analyses suggest that the maximum injected H^- currents from the SCL sheath and the inverse sheath are not very different; hence, the two types of sheath are equally favorable in this aspect.

The total extraction probability of an extraction system is commonly determined by integrating the local extraction probability P_{loc} of an elementary surface area dA, over the entire emissive converter surface [15]:

$$P_{ext} = \int_A P_{loc} \mathrm{d}A, \tag{23}$$

where P_{loc} is the number of extracted H^- over the total number of created H^- for the surface element dA. Such a probability can be measured experimentally or can be predicted by numerical simulations, but direct analytical calculation is, in general, complicated. The extraction probability is usually calculated by performing a 3D simulation of the negative ion source, and is shown to be affected by the converter shape, filter magnetic field, H^- starting energy, neutral pressure, etc [15, 46–48]. For most general applications, the H^- starting energy was proved to significantly affect the extraction probability, shown in figure 10 [15, 46]. For ITER-NBI simulation with both a flat and chamfered converter shape, P_{ext} is shown to decrease with the H^- starting energy from 1 eV and saturates at approximately half the value after the H^- starting energy surpasses 7 eV [15]. The drop is mostly obvious for a H^- starting energy below 3 eV. A similar trend was obtained for a lower H^- starting energy at different radial positions with respect to the central axis [46]. The referenced ITER-NBI simulation has the same electron and ion temperature setup as the present simulation. The effect is explained by a reduced transport path due to a lower ion gyroradius if the H^- have a lower starting energy. Less destructive collisions (neutralization with H^-, electron stripping, detachment, etc) should occur with a shorter path length, which yields a higher extraction probability.

The H^- starting energy is closely related to the sheath structure near the PG. For an SCL sheath, the H^- are accelerated by the sheath, and their starting energy is dictated by the difference between the PG potential and the bulk plasma. In the present simulation, the PG potential is zero and the H^- starting energy at the sheath edge is comparable with 5 eV, which is more than twice the electron temperature. Experimentally, the sheath acceleration can be controlled by adjusting the PG bias.

With an inverse sheath formed near the PG, however, no sheath acceleration appears and all H^- passing through the sheath barrier only have thermal energy with temperature $T_{H-} = 0.8$ eV in the present simulation. The inverse sheath hence features a H^- starting energy lower than that with the SCL sheath by a factor of several times T_e/T_{H-}, which should correspond to significantly improved extraction probability. Note that the present work only focuses on a short distance from the PG surface and studies the sheath physics therein. The present simulation does not consider the realistic filter magnetic field and the H^- collisions, and cannot directly describe the exact H^- transport to the extraction grid. The descriptions of how the H^- entering energy affects its extraction probability are based on previous works that consider the complete extraction region, where the H^- entering energy was given as a constant by disregarding the PG sheath region and simplifying it as a boundary. Our future simulation involving a more complete extraction region is expected to further investigate the H^- transport in the extraction region when an inverse sheath is formed in front of the PG surface.

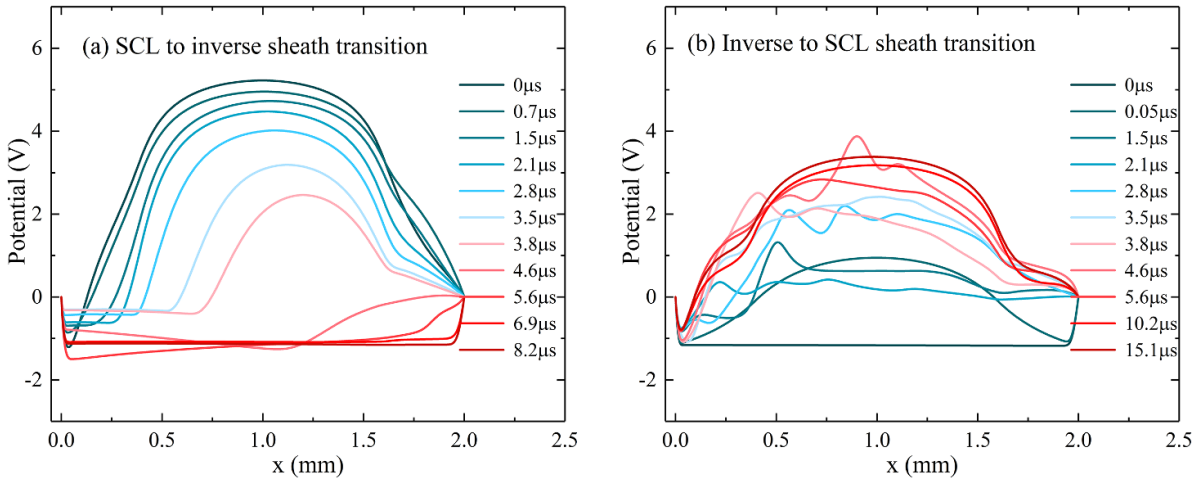

Figure 11. The transition between an electronegative SCL sheath and an inverse sheath. In (*a*), the simulation begins with a converged SCL sheath achieved with a 0.1 m H^+ charge-exchange collision mean free path, and the mean free path is decreased to 0.02 m to trigger the transition to the inverse sheath. In (*b*), the simulation begins with a converged inverse sheath achieved with a 0.02 m mean free path, and the mean free path is decreased to 0.1 m to trigger the transition to the SCL sheath. An artificial strong plasma fueling source is added in the first 3.5 μs to provide sufficient electrons to trigger the transition, which is then replaced with the default plasma fueling rate that is proportional to the H^+ boundary loss. All the other simulation parameters are kept the same.

4. Mode transition between inverse and SCL sheath

In section 3, the advantages and disadvantages of an electronegative inverse and SCL sheath in H^- extraction are discussed in detail. In reality, it is crucial to determine which type of sheath is actually formed in front of the PG and estimate the injected H^- conditions and the bulk plasma properties, considering that the inverse sheath and SCL sheath are coupled with significantly different plasma density distributions. In this section, the transition between a classic, inverse, and SCL sheath for the electronegative plasma is expatiated, offering dedicated approaches to achieve the desired plasma-sheath coupling.

The transition between the SCL sheath and inverse sheath can be triggered by the change in the H^+ charge-exchange collision rate near the boundary. A stable SCL sheath can only be formed when no excessive numbers of cold H^+ produced by charge-exchange collision are accumulated near the PG. For an SCL sheath, the plasma flux balance at the PG is as follows:

$$\Gamma_{\rm i}^{\rm w} = \Gamma_{\rm np}^{\rm w} + \Gamma_{\rm nb,ref}^{\rm w} - \Gamma_{\rm nb}^{\rm w} + \Gamma_{\rm e}^{\rm w}. \tag{24}$$

The difference between equations (24) and (10) is that here an extra electron flux term toward the PG $\Gamma_{\rm e}^{\rm w}$ is involved. The wall electron flux depends on the potential difference between the VC potential minimum and the SCL sheath edge, $\varphi_{\rm vc-se} \geqslant 0$, with $\Gamma_{\rm e}^{\rm w} = \Gamma_{\rm e,se}\exp(-\frac{e\varphi_{\rm vc-se}}{T_{\rm e}})$. The wall-emitted H^- net flux is $\Gamma_{\rm nb,ref}^{\rm w} - \Gamma_{\rm nb}^{\rm w} = -\Gamma_{\rm nb}^{\rm w}\exp(-\frac{e\varphi_{\rm vc-w}}{T_{\rm i}})$, where $\varphi_{\rm vc-w} \geqslant 0$ is the potential difference between the VC and the PG. When the cold H^+ accumulate in the VC due to charge-exchange collision, the VC potential dip is undermined such that all the terms on the RHS of equation (24) are perturbed and a flux balance can no longer be maintained. This drives a transition to the inverse sheath, shown in figure 11(*a*). Here, a simulation is performed, which starts with a converged SCL sheath case achieved with a H^+ charge-exchange collision mean free path of 0.1m, and then the charge-exchange collision mean free path is reduced to 0.02 m in the entire simulation domain from $t = 0$ s. The SCL sheath gradually collapses and eventually forms a stable inverse sheath with ion–ion plasma and few electrons in the plasma. A transition from the converged inverse sheath to an SCL sheath is also tested. The converged inverse sheath was achieved with a 0.02 m charge-exchange collision mean free path, and then the mean free path is increased to 0.1 m to trigger the transition to the SCL sheath. Because the plasma fueling rate of the electron–H^+ pair in the fueling region is proportional to the H^+ boundary loss, which is low for a converged inverse sheath case, an artificial strong fueling source is added in the first 3.5 μs of the simulation to provide enough electrons to trigger the transition to the SCL sheath. The artificial source is replaced with the default fueling rate after 3.5 μs and, eventually, a stable inverse sheath is formed. The final converged sheath potential is slightly different from figure 2(*b*) due to the different plasma density caused by the artificial fueling.

A scan of the H^+ charge-exchange collision mean free path $\lambda_{\rm CX}$ is performed to further develop the above transition between an electronegative SCL and inverse sheath, shown in figure 12. All runs begin with the default initial conditions. A sharp transition from the inverse sheath to the SCL sheath occurs when $\lambda_{\rm CX}$ approaches 0.1 m, which is five times the $\lambda_{\rm CX}$ chosen by default and corresponds to a much lower neutral pressure. The plasma potential is below the PG potential in the inverse sheath cases and is above the PG potential after the transition to the SCL sheath when increasing the $\lambda_{\rm CX}$. The normalized electron density in bulk plasma also rises significantly from almost zero to approximately 70% after the transition. Here, the point with the lowest $\lambda_{\rm CX} = 0.02$ m is the value adopted for all simulations in the previous sections. The value

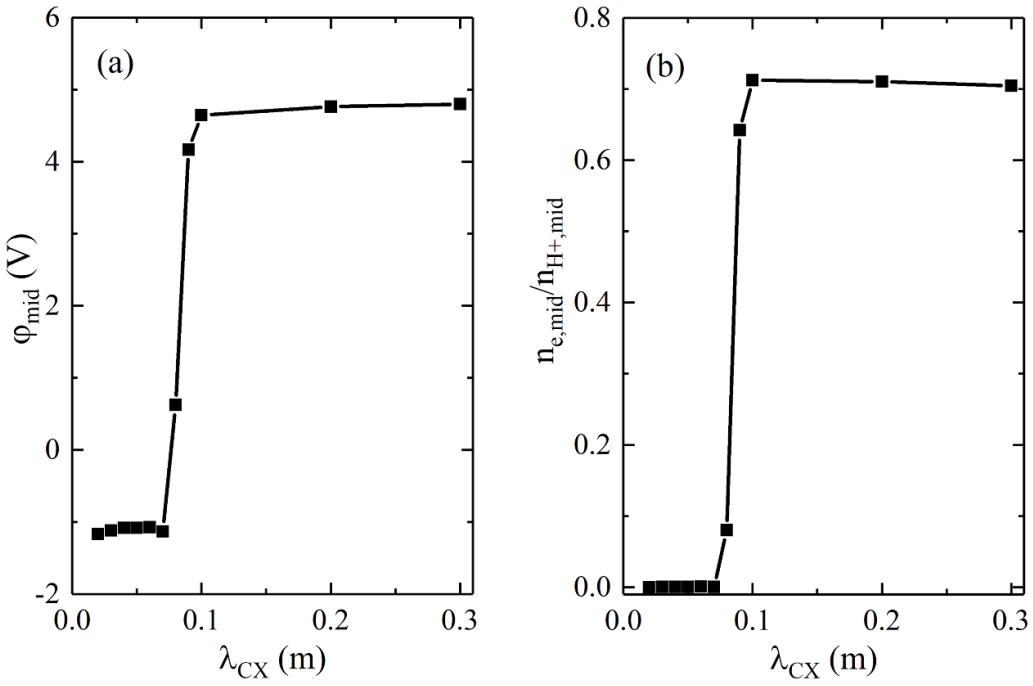

Figure 12. Scans of the H^+ charge-exchange collision mean free path for (*a*) the mid-plane potential and (*b*) electron density normalized by H^+ density in the mid-plane. Note that the boundaries are grounded so that the mid-plane potential is negative if an inverse sheath is formed, and is positive for an SCL sheath.

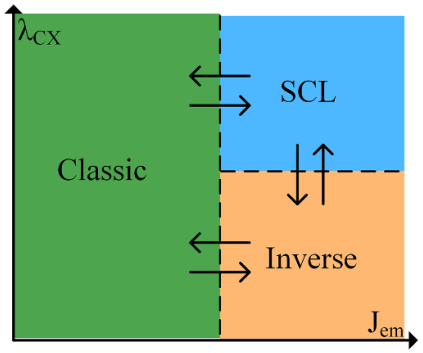

Figure 13. A schematic of a phase diagram representing the transition between a classic non-emissive electronegative sheath, an SCL sheath and an inverse sheath, due to the change in the H^- emission current at the PG and the H^+ charge-exchange collision mean free path.

of the λ_{CX} is calculated to be from 0.016 m to 0.028 m, for a H^+ temperature between 0.03 eV and 2 eV, using the standard source working pressure 0.3 Pa [49]. Hence, it is possible to achieve the inverse sheath at the PG surface of the negative ion source for NBI without changing the existing plasma conditions.

The transition of emissive electronegative sheath modes can be summarized by the phase diagram in figure 13. When increasing the surface H^- emission current above the critical value, high H^+ collisionality yields an inverse sheath and low collisionality leads to an SCL sheath. Decreasing the surface emission restores the sheath back to the classic regime if the H^+ charge-exchange mean free path λ_{CX} is unchanged. An SCL sheath can collapse and transform into the inverse sheath when the sheath becomes more collisional, and a stable inverse sheath can shift into an SCL sheath by increasing the λ_{CX}.

5. Experimental support

The proposed theoretical model, though supported by the continuum kinetic simulation, will be better validated if supported by experiments in a practical NBI system. The potential distribution near the emissive PG surface, however, is rather difficult to be directly diagnosed by, e.g. a Langmuir probe, due to the small size of the sheath (both an electronegative inverse sheath and an SCL sheath). Indirect evidence is much more convenient knowing that the properties of bulk plasma coupled with the inverse sheath and the SCL sheath are fundamentally different: the inverse sheath features a plasma consisting of only positive and negative hydrogen ions, whereas an SCL sheath corresponds to a typical electronegative plasma with considerable electron concentration and, here, the electron density is higher than the H^- density in bulk plasma, figure 3. The bulk plasma properties can be easily measured by the conventional probe diagnostics. It transpires that such ion–ion plasma has been observed near the PG of a negative ion source in experiments, but the causes remain elusive and numerous hypotheses of its formation exist. The proposed electronegative inverse sheath model can ably reproduce the previously observed ion–ion plasma formation.

A first observation was reported on the testbeds of a negative ion source for ITER-NBI at IPP Garching [50], where one Langmuir probe showed a significantly lower current at a positive voltage scan range than expected. With cesium, the probe *I–V* trace is nearly symmetric in positive and negative voltage

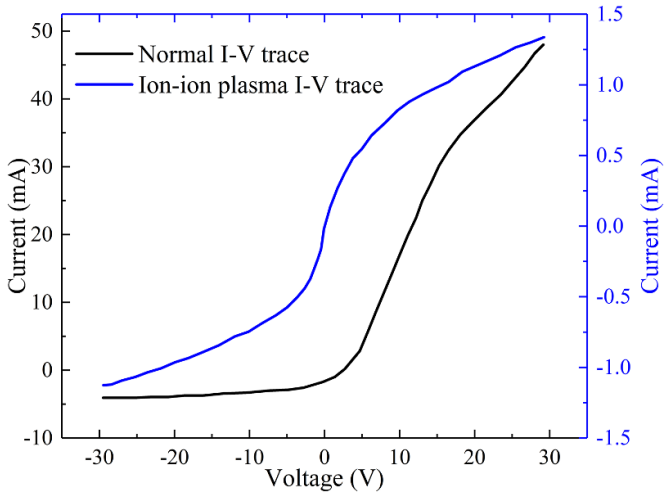

Figure 14. Probe data showing the normal Langmuir probe *I–V* trace and the trace for ion–ion plasma measured by Schiesko *et al* near the PG [51]. Similar traces for ion–ion plasma were also measured in other experiments [50, 52].

branches, suggesting clear evidence of plasma consisting of mainly positive and negative hydrogen ions and few electrons. Such an anomalous *I–V* probe trace was subsequently reproduced in several works with cesium seeding [51, 52]. An example of the symmetrical Langmuir probe *I–V* trace corresponding to the ion–ion plasma is shown in figure 14 [51]. It must be pointed out that factors, such as a PG bias potential, cesium ions, and a magnetic filter field, may also contribute to the formation of the above plasma type [20, 22, 53, 54], which are not included in the present simulation. Further modeling efforts are hence anticipated to incorporate the present model into a more realistic multi-dimensional extraction region simulation, or even coupled with simulation of the entire negative ion source.

It should be noted that the previous probe measurements of the ion–ion plasma formed in front of the PG surface of a negative ion source suggested a positive plasma potential relative to the PG, instead of the negative plasma potential as predicted by the inverse sheath theory. This paradox could be solved by a recent comparison of the same inverse sheath formation in front of the emissive surface using different treatments of electron–neutral collision [25, 26]. With realistic ionizations, positive ions generated in bulk plasma are trapped and accumulate, forming a potential 'hill' in bulk plasma, which leads to a non-flat presheath coupled with the inverse sheath and a positive plasma potential relative to the surface. This is foreseen in front of the PG surface in the present work, but further PIC simulation is expected to validate the hypothesis.

Another way to distinguish the electronegative inverse sheath from the SCL sheath is from the H^- energy. The SCL sheath features strong sheath acceleration, which leads to H^- much faster than with the inverse sheath. But the realistic temperature of H^- just emitted from the surface is also not easily available; therefore, special experiment design is needed to verify the exact sheath structure formed near the PG.

6. Conclusions

The electronegative inverse sheath is proposed as an alternative sheath solution formed in front of the H^--emitting PG in the extraction region of the negative ion source for the NBI system, using the continuum, kinetic simulation, and theoretical analyses. The electronegative inverse sheath features a wall potential floating above the plasma and is coupled with a plasma consisting of only positive and negative hydrogen ions. Contrary to the commonly believed SCL sheath formed near the PG, the inverse sheath features zero sheath acceleration and therefore injects H^- with much lower energy than the SCL sheath into the plasma. H^- injected through the inverse sheath hence encounters less volumetric losses and has higher extraction efficiency. Both simulation results and theoretical analyses suggest that the inverse sheath potential increases with the H^- emission current in a near-logarithmical way, whereas the maximum injected current into plasma via the inverse sheath only depends on the ion temperature. The maximum injected currents from the inverse sheath and SCL sheath are comparable. Transition between the two sheath modes is possible by varying the H^+ charge-exchange collision rate and surface H^- emission flux, which is essentially regulated by the cold H^+ generation and accumulation near the emissive boundary. The predicted ion–ion plasma coupled with the inverse sheath was observed in previous NBI experiments and can possibly justify the existence of an electronegative inverse sheath in the extraction system of a negative ion source. The present theory and modeling results further motivate more complete numerical and experimental tests of the inverse sheath in the negative ion hydrogen source for NBI systems.

Acknowledgments

Guang-Yu would like to thank Dr Ivo Furno, Dr Alan Howling, and Dr Philippe Guittienne at the Swiss Plasma Center, EPFL for fruitful discussions of the simulation model. The research was conducted under the auspices of the National Key R&D Program of China (No. 2020YFC2201100), the National Natural Science Foundation of China (Nos. 51827809, 52077169, 12105041), and the State Key Laboratory of Electrical Insulation and Power Equipment (EIPE22116). This work was supported in part by the Swiss National Science Foundation.

ORCID iDs

Guang-Yu Sun https://orcid.org/0000-0001-6761-6019
Wei Yang https://orcid.org/0000-0002-0179-7854
Jian Chen https://orcid.org/0000-0001-9807-489X
Hao-Min Sun https://orcid.org/0000-0001-7403-6450
Bao-Hong Guo https://orcid.org/0000-0001-8368-5014

Shu Zhang https://orcid.org/0000-0001-9366-7426
Ying-Han Wang https://orcid.org/0009-0004-5888-2277
An-Bang Sun https://orcid.org/0000-0003-1918-3110
Guan-Jun Zhang https://orcid.org/0000-0003-1859-0443

References

[1] Hopf C., Starnella G., den Harder N. and Fantz U. 2021 Neutral beam injection for fusion reactors: technological constraints versus functional requirements *Nucl. Fusion* **61** 106032
[2] Karpushov A.N. *et al* 2017 Neutral beam heating on the TCV tokamak *Fusion Eng. Des.* **123** 468–72
[3] Sonato P., Agostinetti P., Fantz U., Franke T., Furno I., Simonin A. and Tran M.Q. 2016 Conceptual design of the beam source for the DEMO neutral beam injectors *New J. Phys.* **18** 125002
[4] Karpushov A.N. *et al* 2023 Upgrade of the neutral beam heating system on the TCV tokamak—second high energy neutral beam *Fusion Eng. Des.* **187** 113384
[5] Tae-Seong K. , Seung Ho J. , Doo Hee C. , Kwang Won L. and Sang-Ryul I. 2014 Performance of a new ion source for KSTAR tokamak plasma heating *Plasma Sci. Technol.* **16** 620
[6] Wei J. *et al* 2020 Key issues for the filament-arc ion source of EAST neutral beam injector toward high-power and long-pulse operation *Plasma Phys. Control. Fusion* **62** 025004
[7] Kuriyama M. *et al* 1998 Operation of the negative-ion based NBI for JT-60U *Fusion Eng. Des.* **39–40** 115–21
[8] Kuriyama M. *et al* 2000 Power flow in the negative-ion based neutral beam injection for JT-60 *Rev. Sci. Instrum.* **71** 751–4
[9] Ikeda Y. *et al* 2006 Present status of the negative ion based NBI system for long pulse operation on JT-60U *Nucl. Fusion* **46** S211
[10] Takeiri Y. *et al* 2006 High-power and long-pulse injection with negative-ion-based neutral beam injectors in the Large Helical Device *Nucl. Fusion* **46** S199
[11] Fantz U., Wünderlich D., Riedl R., Heinemann B. and Bonomo F. 2020 Achievement of the ITER NBI ion source parameters for hydrogen at the test facility ELISE and present status for deuterium *Fusion Eng. Des.* **156** 111609
[12] Singh M.J., Boilson D., Polevoi A.R., Oikawa T. and Mitteau R. 2017 Heating neutral beams for ITER: negative ion sources to tune fusion plasmas *New J. Phys.* **19** 055004
[13] McAdams R., Holmes A.J.T., King D.B. and Surrey E. 2011 Transport of negative ions across a double sheath with a virtual cathode *Plasma Sources Sci. Technol.* **20** 035023
[14] McAdams R. and Bacal M. 2010 The negative ion flux across a double sheath at the formation of a virtual cathode *Plasma Sources Sci. Technol.* **19** 042001
[15] Gutser R., Wünderlich D. and Fantz U. 2009 Negative hydrogen ion transport in RF-driven ion sources for ITER NBI *Plasma Phys. Control. Fusion* **51** 045005
[16] Bacal M., Sasao M. and Wada M. 2021 Negative ion sources *J. Appl. Phys.* **129** 221101
[17] Fantz U., Briefi S., Heiler A., Wimmer C. and Wünderlich D. 2021 Negative hydrogen ion sources for fusion: from plasma generation to beam properties *Front. Phys.* **9** 709651
[18] Serianni G. *et al* 2017 Neutralisation and transport of negative ion beams: physics and diagnostics *New J. Phys.* **19** 045003
[19] Campanell M.D. 2018 Alternative model of space-charge-limited thermionic current flow through a plasma *Phys. Rev.* E **97** 043207
[20] Mochalskyy S., Wünderlich D., Fantz U., Franzen P. and Minea T. 2015 Towards a realistic 3D simulation of the extraction region in ITER NBI relevant ion source *Nucl. Fusion* **55** 033011
[21] Sun G.-Y., Zhang S., Guo B.-H., Sun A.-B. and Zhang G.-J. 2022 Vlasov simulation of the emissive plasma sheath with energy-dependent secondary emission coefficient and improved modeling for dielectric charging effects *Front. Phys.* **10**
[22] Nishioka S., Goto I., Miyamoto K., Hatayama A. and Fukano A. 2016 Study of ion-ion plasma formation in negative ion sources by a three-dimensional in real space and three-dimensional in velocity space particle in cell model *J. Appl. Phys.* **119** 023302
[23] Campanell M.D. and Umansky M.V. 2016 Strongly emitting surfaces unable to float below plasma potential *Phys. Rev. Lett.* **116** 085003
[24] Zhang Z., Wu B., Yang S., Zhang Y., Chen D., Fan M. and Jiang W. 2018 Formation of stable inverse sheath in ion–ion plasma by strong negative ion emission *Plasma Sources Sci. Technol.* **27** 06LT1
[25] Zhang S., Sun G.-Y., Chen J., Sun H.-M., Sun A.-B. and Zhang G.-J. 2022 On the ohmic-dominant heating mode of capacitively coupled plasma inverted by boundary electron emission *Appl. Phys. Lett.* **121** 014101
[26] Sun G.-Y., Sun A.-B. and Zhang G.-J. 2020 Intense boundary emission destroys normal radio-frequency plasma sheath *Phys. Rev.* E **101** 033203
[27] Yip C.-S., Jin C., Zhang W., Xu G.S. and Hershkowitz N. 2020 Experimental investigation of sheath effects on I–V traces of strongly electron emitting probes *Plasma Sources Sci. Technol.* **29** 025025
[28] Wang X., Pilewskie J., Hsu H.W. and Horányi M. 2016 Plasma potential in the sheaths of electron-emitting surfaces in space *Geophys. Res. Lett.* **43** 525–31
[29] Kraus B.F. and Raitses Y. 2018 Floating potential of emitting surfaces in plasmas with respect to the space potential *Phys. Plasmas* **25** 030701
[30] Wünderlich D., Gutser R. and Fantz U. 2009 PIC code for the plasma sheath in large caesiated RF sources for negative hydrogen ions *Plasma Sources Sci. Technol.* **18** 045031
[31] Fukano A. and Hatayama A. 2013 Analysis of plasma distribution near the extraction region in surface produced negative ion sources *Rev. Sci. Instrum.* **85** 02B123
[32] Etoh H. *et al* 2016 Study of H^- production in DC H^- source of medical cyclotron *Plasma Fusion Res.* **11** 2406063
[33] Fantz U., Falter H., Franzen P., Wünderlich D., Berger M., Lorenz A., Kraus W., McNeely P., Riedl R. and Speth E. 2006 Spectroscopy—a powerful diagnostic tool in source development *Nucl. Fusion* **46** S297
[34] Fukano A. and Hatayama A. 2019 Analysis of plasma distribution near the extraction region in negative ion sources with surface and volume produced negative ions *Plasma Fusion Res.* **14** 3403096
[35] Colonna G. 2016 Boltzmann and Vlasov equations in plasma physics *Plasma Modeling* (IOP Publishing) pp 1–23
[36] Bhatnagar P.L., Gross E.P. and Krook M. 1954 A model for collision processes in gases. I. Small amplitude processes in charged and neutral one-component systems *Phys. Rev.* **94** 511–25
[37] Abrams T. *et al* 2021 Design and physics basis for the upcoming DIII-D SAS-VW campaign to quantify tungsten leakage and transport in a new slot divertor geometry *Phys. Scr.* **96** 124073
[38] Fantz U. and Wünderlich D. 2006 A novel diagnostic technique for H−(D−) densities in negative hydrogen ion sources *New J. Phys.* **8** 301
[39] Sun G.-Y., Li H.-W., Sun A.-B., Li Y., Song B.-P., Mu H.-B., Li X.-R. and Zhang G.-J. 2019 On the role of secondary electron emission in capacitively coupled radio-frequency

plasma sheath: a theoretical ground *Plasma Process. Polym.***16** 1900093
[40] Meyer M., Nayak G., Bruggeman P.J. and Kushner M.J. 2022 Sheath formation around a dielectric droplet in a He atmospheric pressure plasma *J. Appl. Phys.* **132** 083303
[41] Chabert P. 2014 What is the size of a floating sheath? *Plasma Sources Sci. Technol.* **23** 065042
[42] Van Wunnik J.N.M., Geerlings J.J.C. and Los J. 1983 The velocity dependence of the negatively charged fraction of hydrogen scattered from cesiated tungsten surfaces *Surf. Sci.* **131** 1–16
[43] Rasser B., Van Wunnik J.N.M. and Los J. 1982 Theoretical models of the negative ionization of hydrogen on clean tungsten, cesiated tungsten and cesium surfaces at low energies *Surf. Sci.* **118** 697–710
[44] Van Wunnik J.N.M., Geerlings J.J.C., Granneman E.H.A. and Los J. 1983 The scattering of hydrogen from a cesiated tungsten surface *Surf. Sci.* **131** 17–33
[45] Lee B.S. and Seidl M. 1992 Surface production of H^- ions by hyperthermal hydrogen atoms *Appl. Phys. Lett.* **61** 2857–9
[46] Matsumoto Y., Nishiura M., Shinto K., Yamaoka H., Sasao M. and Wada M. 2010 Influence of H^- velocity on H^- extraction probability from a negative ion source *Rev. Sci. Instrum.* **81** 02B701
[47] Matsumoto Y., Nishiura M., Matsuoka K., Sasao M., Wada M. and Yamaoka H. 2006 Dependence of H− extraction probability on filter magnetic field and gas pressure of a volume-type negative ion source *Thin Solid Films* **506–507** 522–6
[48] Fubiani G., Garrigues L., Hagelaar G., Kohen N. and Boeuf J.P. 2017 Modeling of plasma transport and negative ion extraction in a magnetized radio-frequency plasma source *New J. Phys.* **19** 015002
[49] Lindsay B.G. and Stebbings R.F. 2005 Charge transfer cross sections for energetic neutral atom data analysis *J. Geophys. Res.* **110** A12213
[50] McNeely P. and Schiesko L. 2010 Investigation of fringe plasma parameters on a high power rf driven ion source *Rev. Sci. Instrum.* **81** 02B111
[51] Schiesko L., McNeely P., Fantz U. and Franzen P. 2011 Caesium influence on plasma parameters and source performance during conditioning of the prototype ITER neutral beam injector negative ion source *Plasma Phys. Control. Fusion* **53** 085029
[52] Tsumori K. *et al* 2012 Spatial distribution of the charged particles and potentials during beam extraction in a negative-ion source *Rev. Sci. Instrum.* **83** 02B116
[53] Taccogna F., Schneider R., Longo S. and Capitelli M. 2008 Modeling of a negative ion source. II. Plasma-gas coupling in the extraction region *Phys. Plasmas* **15** 103502
[54] Montellano I.M., Wünderlich D., Mochalskyy S. and Fantz U. 2019 3D-PIC modelling of a low temperature plasma sheath with wall emission of negative particles and its application to NBI sources *J. Phys. D: Appl. Phys.* **52** 235202